Direct numerical simulations of vortex rings at $Re_\Gamma = 7500$

MICHAEL BERGDORF[1], PETROS KOUMOUTSAKOS[1] AND ANTHONY LEONARD[2]

[1]Computational Science & Engineering Laboratory, ETH Zurich, Switzerland
[2]Graduate Aeronautical Laboratories, California Institute of Technology, Pasadena, USA

We present direct numerical simulations of the turbulent decay of vortex rings with $Re_\Gamma = 7500$. We analyse the vortex dynamics during the nonlinear stage of the instability along with the structure of the vortex wake during the turbulent stage. These simulations enable the quantification of vorticity dynamics and their correlation with structures from dye visualization and the observations of circulation decay that have been reported in related experimental works. Movies are available with the online version of the paper.

1. Introduction

Vortex rings are one of the archetypal structures of fluid dynamics phenomena ranging from fish swimming to oil drilling (see Shariff & Leonard 1992). The instability of vortex rings has been the subject of several theoretical and experimental studies (see Shariff & Leonard 1992 and Shariff, Verzicco & Orlandi 1994). The works of Widnall & Sullivan (1973) and Widnall, Bliss & Tsai (1974) identified an instability mechanism due to small sinusoidal perturbation of the vortex ring centreline. They quantified the number of waves around the perimeter of the ring and demonstrated qualitative agreement with their experimental measurements of vortex rings in air. Shariff *et al.* (1994) performed finite-difference calculations of the linear and early nonlinear stage of rings of varying Reynolds number. They reproduced the azimuthal instability and observed the amplification of mean swirl in the early nonlinear stage. Beyond the nonlinear stage, Weigand & Gharib (1994) performed particle image velocimetry (PIV) measurements of the decay of a $Re_\Gamma = 7500$ vortex ring, where Re_Γ is the Reynolds number based on the circulation, and found that the circulation of the core decays in a stepwise manner. They attributed this behaviour to a periodic ejection of vortices into the wake of the vortex ring. Recently, Dazin *et al.* have presented experimental investigations of the linear (see Dazin, Dupont & Stanislas 2006*a*), and nonlinear stage (see Dazin, Dupont & Stanislas 2006*b*) of vortex ring decay. In these studies, they characterize the instability during the nonlinear stage using laser cuts through the vortex and by performing a Fourier analysis on the azimuthal velocity. This analysis suggests a transfer of energy from the unstable modes of the linear stage to its second harmonics.

The goal of the present computational study is to clarify the three-dimensional vortex dynamics during the nonlinear stage and determine the structure of the wake in the turbulent stage.

We present the numerical method in §2, and define the setup of the simulation in §3. We then focus on the dynamics of the formation of secondary vortex structures

in §4. Section 5 is concerned with the structure of the vortex ring wake and the decay of circulation. Section 6 will summarize and conclude this work.

2. Governing equations and numerical method

We consider the evolution of vortical, incompressible, viscous flows as expressed by the Navier–Stokes (NS) equations in the Lagrangian vorticity form:

$$\frac{\mathrm{D}\boldsymbol{\omega}}{\mathrm{D}t} = (\boldsymbol{\omega}\cdot\nabla)\boldsymbol{u} + \nu\,\Delta\boldsymbol{\omega}, \tag{2.1}$$

and

$$\Delta\boldsymbol{\Psi} = \nabla\times\boldsymbol{u} = -\boldsymbol{\omega}. \tag{2.2}$$

We discretize these equations in a periodic domain using a vortex method (see Cottet & Koumoutsakos 2000; Koumoutsakos 2005). The vorticity field is approximated using a linear superposition of particles,

$$\boldsymbol{\omega}(\boldsymbol{x}, t) \approx \sum_p \Gamma_p(t)\,\zeta_\varepsilon(\boldsymbol{x} - \boldsymbol{x}_p(t)), \tag{2.3}$$

where Γ_p are the particle strengths, $\boldsymbol{x}_p$ the particle locations and ζ_ϵ is a kernel function. The discretization of the NS equations yields a set of ordinary differential equations (ODE) for the particle positions and their circulation:

$$\frac{\mathrm{d}\Gamma_p}{\mathrm{d}t} = v_p(\boldsymbol{\omega}\cdot\nabla^h)\boldsymbol{u} + \nu\,\Delta^h\Gamma_p, \qquad \frac{\mathrm{d}\boldsymbol{x}_p}{\mathrm{d}t} = \boldsymbol{u}(\boldsymbol{x}_p, t), \tag{2.4}$$

where $v_p = h^3$ are the particle volumes. The ODEs (2.4) are integrated using a third-order low-storage Runge–Kutta method (see Williamson 1980). The particles are remeshed at each time step onto a regular grid in order to alleviate spurious vortical structures generated by their Lagrangian distortion (see Koumoutsakos 1997). The velocities are computed through vorticity in spectral space, while the stretching term and the viscous term are evaluated using centred fourth-order-accurate finite differences. The present code is a parallel application implemented using the Parallel Particle Mesh Library (see Sbalzarini *et al.* 2006). Advantages of hybrid vortex methods include stability (no CFL restriction) and negligible numerical dissipation and dispersion errors. For nonlinear stability the time step must satisfy $\delta t \leqslant C\,\|\nabla\otimes\boldsymbol{u}\|_\infty^{-1}$, where C is a constant depending on the ODE solver used. In the present simulations we use an adaptive time step of size $\delta t = 0.125\,\|\boldsymbol{\omega}\|_\infty^{-1}$ and use $\zeta(\boldsymbol{x}) = M_4'(x)\,M_4'(y)\,M_4'(z)$ with $\varepsilon = h$. For a more detailed description of the method and kernel refer to Sbalzarini *et al.* (2006), Cottet & Koumoutsakos (2000) and Koumoutsakos (2005).

3. Setup

Following Shariff *et al.* (1994), we use a Gaussian ring as initial condition:

$$\omega_\theta(\boldsymbol{x}, t = 0) = \frac{\Gamma}{\pi\sigma^2}\,\mathrm{e}^{-(s/\sigma)^2}, \tag{3.1}$$

with $s^2 = (z - z_c)^2 + (|(x, y) - (x_c, y_c)| - R)^2$, and $R = 1.4\,\mathrm{cm}$ (see figure 1). Unless stated otherwise, variables are dimensionless and have been transformed as

$$t = \frac{\Gamma}{R^2}\,\tilde{t}, \qquad x = \frac{1}{R}\,\tilde{x}, \qquad \boldsymbol{\omega} = \frac{R^2}{\Gamma}\,\tilde{\boldsymbol{\omega}}.$$
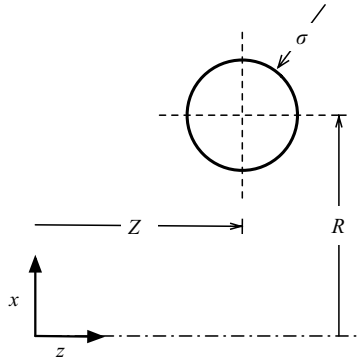
FIGURE 1. Initial setup; R denotes the vortex ring radius, σ is the ring thickness and Z locates the position of maximum vorticity.
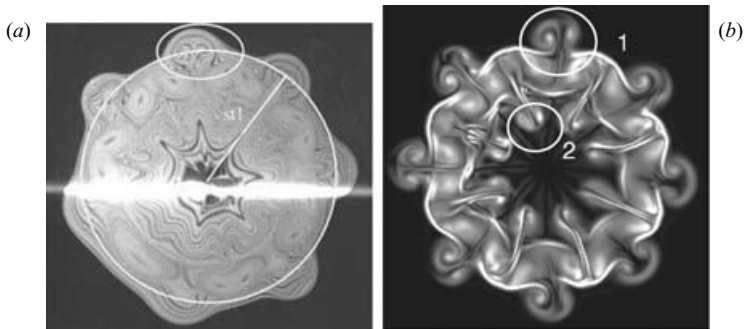

FIGURE 2. (*a*) Dye visualization of the secondary structures in the experiment (reproduced from Dazin *et al.* 2006*b*). (*b*) Vorticity magnitude in the present simulation (1: outer dipoles, 2: inner dipoles).

We superimpose a secondary vortex ring with a Gaussian of opposite vorticity as in Shariff *et al.* (1994) in order to make the total vorticity field vanish at the ring axis. We have used two different values for σ: $\sigma = R/2.4232$ (ring A), and $\sigma = R/3.523$ (ring B), corresponding to $\|\boldsymbol{\omega}\|_\infty(t=0)$ of $69\,\mathrm{s}^{-1}$ and $156\,\mathrm{s}^{-1}$, respectively. The centreline of the ring is randomly perturbed with an amplitude of 0.01. We perform a Helmholtz projection step after the perturbation to enforce a divergence-free vorticity field. The circulation-based Reynolds number is $Re_\Gamma = \Gamma/\nu = 7500$, and $\nu = 10^{-6}\,\mathrm{m}^2\,\mathrm{s}^{-1}$. The size of the computational domain was $[H, H, L]$ with $H = 5.57$ and $L = 22.29$, subject to periodic boundary conditions on all faces. The ring was initially centred at $\boldsymbol{x}_c = (H/2, H/2, 0.0)$. The simulations employed 131 million (A) and 256 million (B) particles, respectively. This corresponds to a grid size of $321 \times 321 \times 1281$ (A) and $401 \times 401 \times 1601$ (B), respectively.

4. Secondary vortices

The main instability mechanism of vortex rings is an azimuthal instability, often referred to as the Tsai–Widnall instability, Widnall instability, or Azimuthal instability. It leads to an extensive bending of the initially circular vortex lines. Experimental studies of vortex rings, at moderate Reynolds numbers, report the onset of the formation of secondary vortical structures, identified in spanwise laser cuts as dipoles on the outer and inner ring circumference (figure 2).
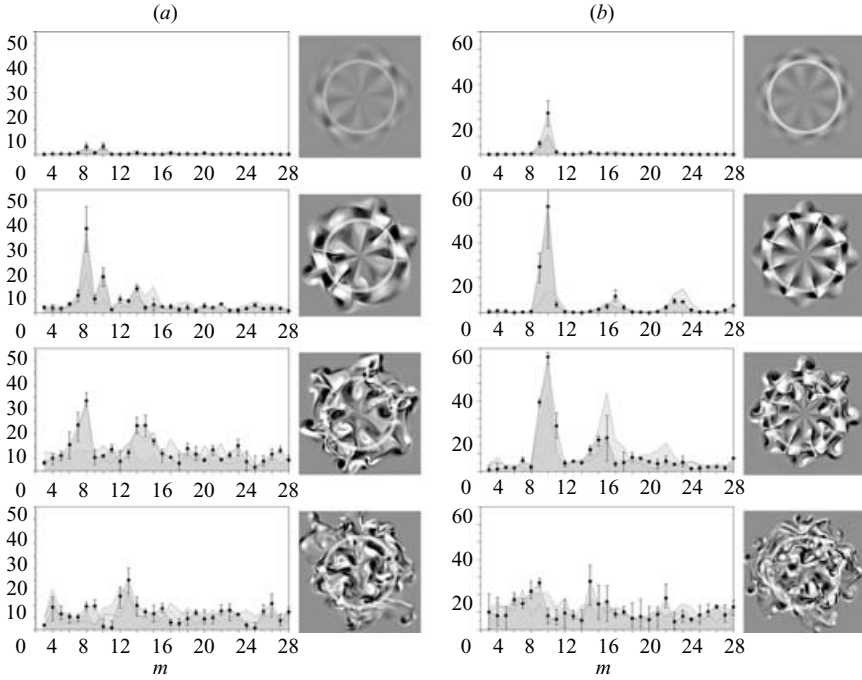
FIGURE 3. (*a*) Ring A, (*b*) ring B; development of the first 30 harmonics. The three different shades in the spectra represent three different measuring planes $z - 0.011$, z, $z + 0.011$. Error bars indicate variation in the radial direction. The corresponding ω_z structures are depicted on the right-hand side of the spectra. The three white circles represent the three measurement radii. Times are $t = 92.75, 125.7, 141.7, 167.0$ for ring A, and $t = 66.66, 84.68, 92.45, 115.2$ for ring B (top to bottom).

In order to investigate the development of the instability – from primary to secondary vortex structures – we have followed an approach employed in Dazin *et al.* (2006*b*): we perform an *XY*-cut through the centre of the ring and measure ω_z on circles concentric with the ring. We then perform a Fourier transform of these data and measure the amplitudes of the first 30 modes. Even at this early stage of the evolution of the vortex ring the notion of the 'centre' and core are subject to interpretation. We therefore measure the modes at three different *Z* slices (z, $z \pm 0.011$) and at three different radii (0.96, 1.00, 1.11). Figure 3(*b*) depicts the evolution of the amplitude of the modes for ring B: streamwise vorticity appears with the onset of the Widnall instability which is apparent in the excitation of the linear unstable mode $m = 8$. With the evolution of the secondary vortex structures, energy is transferred to the second and third harmonics $m = 16$ and $m = 24$. On the transition to turbulence we observe an amplification of the low-order modes. These observations are in agreement with the findings in the experimental study of Dazin *et al.* (2006*b*). Additionally, they observe a mean azimuthal velocity in their experiments. This is a phenomenon, which was the focus of Naitoh *et al.* (2002), where either an $m = 0$, or $m = 1$ mode was observed, depending on the initial perturbation of the ring. In both our simulations we observe an $m = 1$ mode, while the $m = 0$ mode was found to be at least one order of magnitude weaker throughout.

The spectra of the thicker ring A show a qualitatively identical behaviour (see figure 3*a*). However, owing to its thickness the linear unstable modes are found to
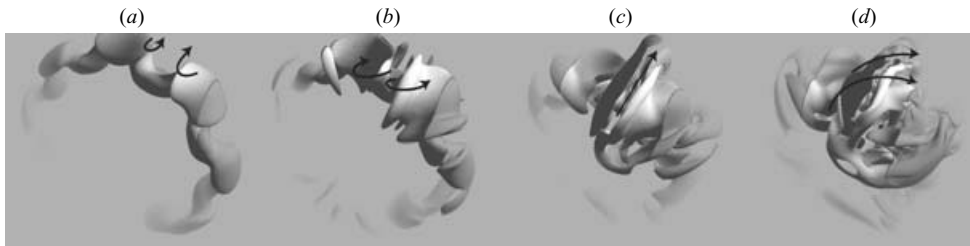
FIGURE 4. Emergence of the secondary vortical structures (*a*–*d*): the Tsai–Widnall, or shortwavelength instability leads to the formation of a dipole which is stretched and convected in the streamwise direction.
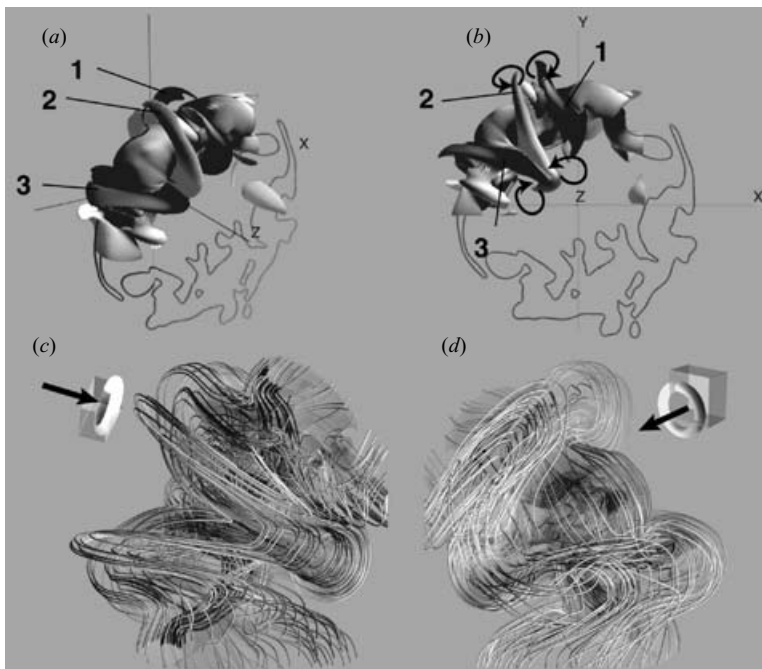

FIGURE 5. Pictures (*a*) and (*b*) depict how the two dipole structures observed in spanwise laser cuts are part of the same structure. The numbers 1, 2 and 3 denote three different tubular structures with alternating sign of ω_z. Pictures (*c*) and (*d*) represent the underlying vortex lines structure for a quarter of the ring.

be $m = 6$ and $m = 8$. Additionally, the amplification of the third harmonics is less apparent.

By inspection of the evolution of the three-dimensional topology of vorticity isosurfaces we discern the following mechanism leading to the secondary vortical structures displayed in figure 4: (*a*) The streamwise rims of the saddles are areas of increased streamwise vorticity (ω_z); (*b*) This ω_z is amplified due to local stretching leading to more pronounced streamwise structures. (*c*) Eventually pairs of oppositely signed streamwise structures that emanate from adjacent saddles approach each other and form streamwise dipoles. These dipoles are stretched downstream by the large-scale velocity field induced by the ring, leading to a marked streamwise alignment. (*d*) The dipoles eventually lose coherence due to axial instability, or due to the dominance of one pole, as indicated by the arrows. As established in figure 5, the

FIGURE 6. Schematic illustration of the main vortex line structure of vortex B during the nonlinear stage: depicted are inner, core, and outer vortex lines, giving rise to the secondary vortices (1: outer dipoles, 2: inner dipoles).
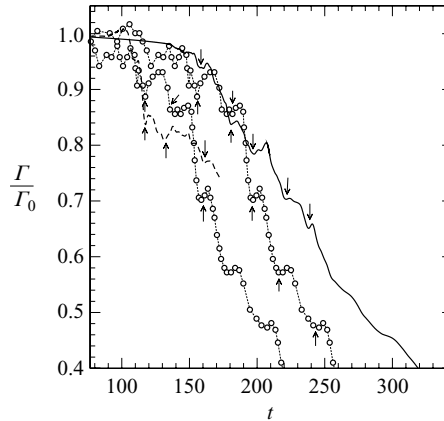

FIGURE 7. Half-plane circulation: ring A (solid line), ring B (dashed line), and experiment Weigand & Gharib (1994) (connected circles). The experimental data have been shifted to match the time of the onset of the decay. Arrows indicate decay plateaus.

dipoles that can be identified in the inner circumference of the ring (figure 2) are part of the same structure as the outer dipoles. However, they are formed by streamwise vorticity structures emanating from the same saddle. Figure 6 depicts a simplified representation of the structure of the vortex rings during the nonlinear stage for the case where $m = 8$ is the dominant linear mode.

5. Decay of circulation

The stepwise decay of circulation during the turbulent evolution of a vortex ring was first reported in experiments by Weigand & Gharib (1994). In figure 7 we report the temporal evolution of the circulation of the vortex rings A, B along with the experimental results Weigand & Gharib (1994). The circulation was computed in the $(y = H/2)$-plane as

$$\Gamma = \tfrac{1}{2} \iint_{A^+} \omega_y \, \mathrm{d}x \, \mathrm{d}z - \tfrac{1}{2} \iint_{A^-} \omega_y \, \mathrm{d}x \, \mathrm{d}z,$$

with $A^+ = [H/2, H] \times L$ and $A^- = [0, H/2] \times L$. In Weigand & Gharib (1994) the circulation was computed as the line integral of the velocity along the $\omega_y \pm 0.065$ contour, not including structures in the wake. We can therefore only qualitatively compare these results; as we compute the circulation in the whole domain, i.e.
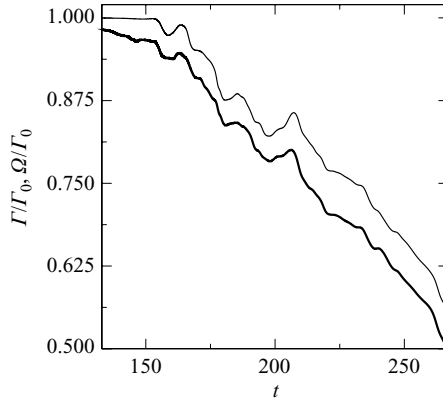
FIGURE 8. Evolution of $\Omega(t)$ (thin solid line), which represents the inviscid decay of Γ (bold solid line), for ring A.

including the wake, we expect the measurement to present a somewhat attenuated representation of the circulation dynamics of the 'core' regions. Additionally, the present simulations were performed at a slightly lower Reynolds number: if we computed the circulation as in Weigand & Gharib (1994) we estimate that we would obtain a Reynolds number around $Re_\Gamma = 7300$ for ring A, and $Re_\Gamma = 7400$ for ring B, respectively. We observe a circulation decay with stepwise character similar to the experimental measurements, albeit less pronounced. For ring A we can identify an agreement of the decay 'frequency' (arrows in figure 7). Additionally, we calculated

$$\frac{\mathrm{d}\Omega}{\mathrm{d}t} = \frac{\mathrm{d}\Gamma}{\mathrm{d}t} - \text{viscous terms}$$

$$= \int (\omega_y u_x - \omega_x u_y)_{x=H/2, y=H/2} \, \mathrm{d}z, \tag{5.1}$$

which represents the inviscid contribution to the circulation decay (Leonard & Reynolds 1988). From equation (5.1) we obtain $\Omega(t)$ through numerical integration. We compare this inviscid decay of circulation to the full circulation $\Gamma(t)$ in figure 8, and observe that the initial decay of circulation, before the initiation of the turbulent stage, is completely viscous. On the other hand, the subsequent stepwise decay of the circulation can be attributed to inviscid mechanisms.

To quantify the strength of vortical structures in the wake we first define the wake domain as

$$A^{\mathrm{w}} = A^+ \backslash \left\{ [H/2, H] \times \left[Z - \tfrac{3}{2}R, Z + \tfrac{3}{2}R \right] \right\},$$

and introduce the following measures:

$$\Sigma_y = \iint_{A^{\mathrm{w}}} |\omega_y| \, \mathrm{d}x \, \mathrm{d}z, \tag{5.2}$$

$$\Sigma_z = \iint_{A^{\mathrm{w}}} |\omega_z| \, \mathrm{d}x \, \mathrm{d}z. \tag{5.3}$$

Figure 9 depicts the evolution of these quantities compared to the decay of circulation for ring A. We observe a burst-like increase in Σ_z and Σ_y concurrent with the decay of circulation. We also find that, starting with the nonlinear phase, Σ_z becomes
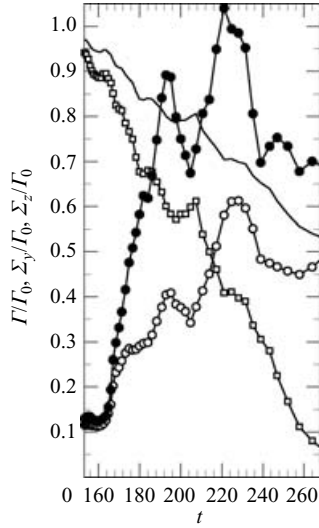
FIGURE 9. Evolution of wake vorticity for ring A: x-vorticity (5.2) ($\circ$), z-vorticity (5.3) ($\bullet$), circulation Γ (——) and ($2\Gamma - 1$) ($\square$).
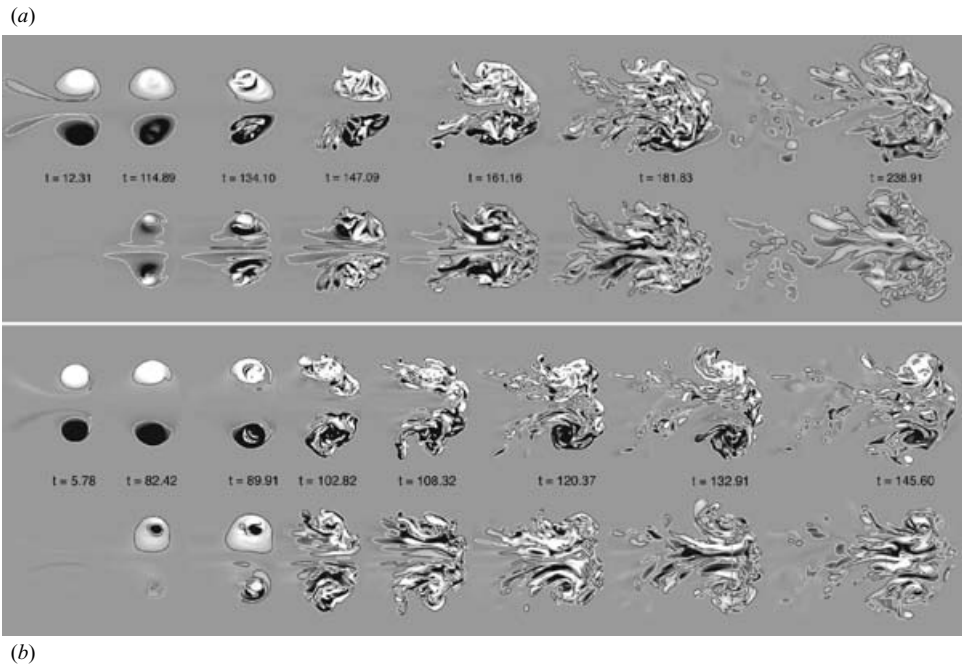
(*a*)

(*b*)

FIGURE 10. Streamwise cuts through the centre of ring A (*a*) and B (*b*). The upper part shows ω_y, that is vorticity perpendicular to the paper plane. Contour lines denote $\omega_y = \pm 0.065$ (A) and $\omega_y = \pm 0.146$ (B), respectively. The lower part shows the streamwise vorticity ω_z and contour lines denote $\omega_z = \pm 0.065$ (A), and $\omega_z = \pm 0.146$ (B), respectively.

dominant compared to Σ_y. We take crosscuts of ω_y and ω_z (A: figure 10*a*†, and B: figure 10*b*), and observe an increased number of streamwise structures when the rings

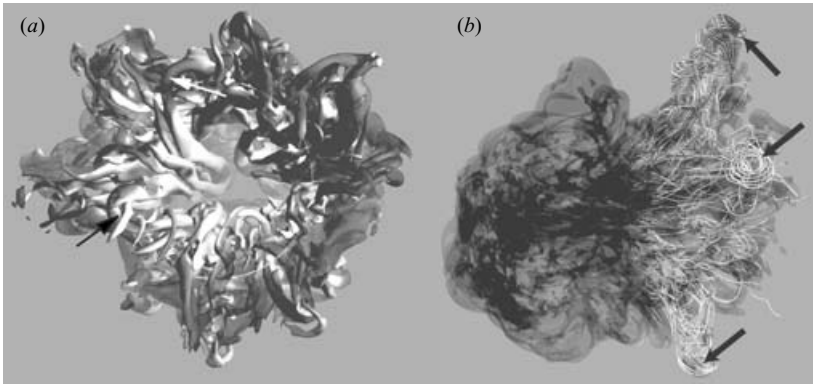† A movie is also available with the online version of the paper (movie 1).

FIGURE 11. (*a*) Isosurface of $|\boldsymbol{\omega}| = 1.7$ for ring B at $t = 108.29$ (viewed from behind). The surface is coloured by the strength of streamwise vorticity, where white regions denote high $|\omega_z|$ and dark ones weak $|\omega_z|$ respectively. Arrows denote hairpin vortices shed from the inside of the turbulent core. (*b*) Isosurface of $|\boldsymbol{\omega}| = 0.41$ for ring B at $t = 120.53$. Arrows denote the ring-like structures in the wake of the vortex.

start decaying. This streamwise vorticity consists of axial structures shed along the wake of the ring and larger-scale vortex structures that are still attached to the inside of the rings. In figure 11(*a*) we examine the isosurface of the strength of vorticity at the beginning of the turbulent phase and identify the above-mentioned attached structures as large-scale hairpin vortices, which are remainders of the secondary vortical structures. As these hairpin vortices are convected into the wake they form ring-like structures at their tip (see figure 11*b*‡). These structures are then shed into the low-speed area off the centre-axis of the ring. At later times the shed vortices become of smaller scale and we observe a clear separation of wake areas (including the inside of the ring) characterized by high $|\omega_z|$, and ring areas, characterized by high $|\omega_y|$ in figure 10. This separation is less pronounced for ring A due to its thicker ring radius.

The above observations of the structure of vorticity, together with the measurements of Σ_y and Σ_z corroborate the theory that the stepwise decay of circulation is a reflection of the periodic shedding of hairpin vortices into the wake area.

We have recorded the z location of the ring across the simulation; we identify the ring location with the location of the maximum of $|\boldsymbol{\omega}| = \omega_\infty$. This is a reasonable definition as long as the ring has not become turbulent. Owing to the different ω_∞ of rings A and B, they assume different maximum translation velocities of 15.68 and 19.60, respectively. The ω_∞ of ring B has been chosen so as to attain the same translation velocity as the ring in Weigand & Gharib (1994). Figure 12(*a*) shows a comparison of the trajectories of A, B and Weigand & Gharib (1994). The trajectory of A has been scaled to match the same maximum translation velocity. In the initial phase we observe reasonable agreement with the experiment, although we find sublinear trajectories for the computations, following

$$z \sim t^{0.925}.$$

This deviation may be attributed to the effect of the periodic images of the rings. Incidentally we find that $z \sim t^{1.05}$ fits the data of Weigand & Gharib (1994) more

‡ A movie is also available with the online version of the paper (movie 2).
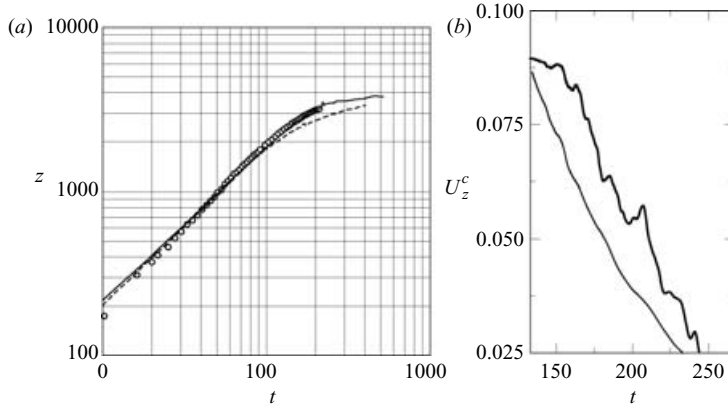
FIGURE 12. (a) Temporal evolution of the ring position, measured as the location of the maximum of $|\omega|$. Circles denote the experiment Weigand & Gharib (1994), the solid line corresponds to ring A (scaled), and the dashed line to ring B. (b) U_z^c of ring A (thin solid line), and Γ (bold solid line). The values of Γ have been scaled to allow a qualitative comparison of the decay.

reliably than $z \sim t$. It must be noted however, that the definition of the centre of the corex of the ring is arguable even during the linear phase. The maximum error in the effective viscosity (Winckelmans & Leonard 1993) of simulation B was found to be 5% at $t \approx 111.0$. This, together with the slightly premature transition to turbulence, may indicate that the simulation of ring B is not fully resolving all scales at all times.

We measured the vorticity-centroid velocity as given by Saffman (1992):

$$U^c = \frac{1}{2} \frac{d}{dt} \int \frac{x \times \omega}{|I|^2} \cdot I \, dv, \qquad (5.4)$$

where I is the impulse of the vortex ring. As we are only interested in the z-component of the centroid velocity, the above expression is reduced and rewritten as

$$U_Z^c = \frac{1}{2} \left(\int \frac{x \omega_y - y \omega_x}{I} u_z \, dv - \frac{1}{2} \int \frac{u_x^2 + u_y^2 - u_z^2}{I} \, dv \right). \qquad (5.5)$$

The velocity (5.5) for ring A is plotted in figure 12(b), together with the decay of the circulation Γ. We observe a series of bumps in the decaying velocity with the same frequency as the stepwise drops of circulation: these bumps are not very pronounced as the centroid velocity (5.5) also accounts for the contribution of the wake.

6. Conclusions

We have presented results from the direct numerical simulation of vortex rings at $Re_\Gamma = 7500$. The availability of the full three-dimensional vorticity field enables us to elucidate the origin and topology of the secondary vortex structures during the nonlinear stage of vortex ring decay. We observe the same stepwise decay of circulation as reported in experimental studies, and observe large-scale hairpin vortices in the wake of the ring during the early turbulent stage. These large-scale vortices are remainders of the secondary vortex structures. Towards the late turbulent stage these structures become larger in number and more small-scale in size.

The present work focuses on the implementation of particle methods with spatially varying core sizes (see Cottet, Koumoutsakos & Ould Salihi 2000; Bergdorf, Cottet & Koumoutsakos 2005) and multi-resolution simulations (Bergdorf & Koumoutsakos 2006) for the simulation of higher Reynolds number vortex rings. These simulations will help us to establish whether there exists an inertial subrange for vortex rings. In the future, ensembles of vortex rings will be considered in order to investigate similarity properties, distributions of mean vorticity, turbulent energy and other quantities (see Glezer & Coles 1990).

REFERENCES

BERGDORF, M., COTTET, G.-H. & KOUMOUTSAKOS, P. 2005 Multilevel adaptive particle methods for convection-diffusion equations. *Multiscale Model. Simul.* **4** (1), 328–357.

BERGDORF, M. & KOUMOUTSAKOS, P. 2006 A Lagrangian particle-wavelet method. *Multiscale Model. Simul.* **5** (3), 980–995.

COTTET, G.-H. & KOUMOUTSAKOS, P. 2000 *Vortex Methods: Theory and Practice*. Cambridge University Press.

COTTET, G.-H., KOUMOUTSAKOS, P. & OULD SALIHI, M.-L. 2000 Vortex methods with spatially varying cores. *J. Comput. Phys.* **162**, 164–185.

DAZIN, A., DUPONT, P. & STANISLAS, M. 2006a Experimental characterization of the instability of the vortex ring. part i: Linear phase. *Exps. Fluids* **40** (3), 383–399.

DAZIN, A., DUPONT, P. & STANISLAS, M. 2006b Experimental characterization of the instability of the vortex rings. part ii: Non-linear phase. *Exps. Fluids* **41** (3), 401–413.

GLEZER, A. & COLES, D. 1990 An experimental-study of a turbulent vortex ring. *J. Fluid Mech.* **211**, 243–283.

KOUMOUTSAKOS, P. 1997 Inviscid axisymmetrization of an elliptical vortex. *J. Comput. Phys.* **138** (2), 821–857.

KOUMOUTSAKOS, P. 2005 Multiscale flow simulations using particles. *Annu. Rev. Fluid Mech.* **37**, 457–487.

LEONARD, A. & REYNOLDS, W. C. 1988 Turbulence research by numerical simulation. In *Perspectives in Fluid Mechanics* Lecture Notes in Physics, vol. 320 (ed. D. Coles), pp. 113–142. Springer.

NAITOH, T., FUKUDA, N., GOTOH, T., YAMADA, H. & NAKAJIMA, K. 2002 Experimental study of axial flow in a vortex ring. *Phys. Fluids* **14** (1), 143–149.

SAFFMAN, P. G. 1992 *Vortex Dynamics*. Cambridge University Press.

SBALZARINI, I. F., WALTHER, J. H., BERGDORF, M., HIEBER, S. E., KOTSALIS, E. M. & KOUMOUTSAKOS, P. 2006 PPM – a highly efficient parallel particle-mesh library. *J. Comput. Phys.* **215** (2), 566–588.

SHARIFF, K. & LEONARD, A. 1992 Vortex rings. *Annu. Rev. Fluid Mech.* **24**, 235–279.

SHARIFF, K., VERZICCO, R. & ORLANDI, P. 1994 A numerical study of three-dimensional vortex ring instabilities: viscous corrections and early nonlinear stage. *J. Fluid Mech.* **279**, 351–375.

WEIGAND, A. & GHARIB, M. 1994 On the decay of a turbulent vortex ring. *Phys. Fluids* **6** (12), 3806–3808.

WIDNALL, S. E., BLISS, D. B. & TSAI, C. 1974 The instability of short waves on a vortex ring. *J. Fluid Mech.* **66** (01), 35–47.

WIDNALL, S. E. & SULLIVAN, J. P. 1973 On the stability of vortex rings. *Proc. R. Soc. Lond.* A **332**, 335–353.

WILLIAMSON, J. H. 1980 Low-storage Runge-Kutta schemes. *J. Comput. Phys.* **35**, 48–56.

WINCKELMANS, G. S. & LEONARD, A. 1993 Contributions to vortex particle methods for the computation of three-dimensional incompressible unsteady flows. *J. Comput. Phys.* **109** (2), 247–273.